

The effect of the geomagnetic field on cosmic ray energy estimates and large scale anisotropy searches on data from the Pierre Auger Observatory

The Pierre Auger Collaboration

P. Abreu⁷⁴, M. Aglietta⁵⁷, E.J. Ahn⁹³, I.F.M. Albuquerque¹⁹, D. Allard³³, I. Allekotte¹, J. Allen⁹⁶, P. Allison⁹⁸, J. Alvarez Castillo⁶⁷, J. Alvarez-Muñiz⁸⁴, M. Ambrosio⁵⁰, A. Aminaei⁶⁸, L. Anchordoqui¹⁰⁹, S. Andringa⁷⁴, T. Antičić²⁷, A. Anzalone⁵⁶, C. Aramo⁵⁰, E. Arganda⁸¹, F. Arqueros⁸¹, H. Asorey¹, P. Assis⁷⁴, J. Aublin³⁵, M. Ave⁴¹, M. Avenier³⁶, G. Avila¹², T. Bäcker⁴⁵, M. Balzer⁴⁰, K.B. Barber¹³, A.F. Barbosa¹⁶, R. Bardenet³⁴, S.L.C. Barroso²², B. Baughman^{98 f}, J. Bäuml³⁹, J.J. Beatty⁹⁸, B.R. Becker¹⁰⁶, K.H. Becker³⁸, A. Bellétoile³⁷, J.A. Bellido¹³, S. BenZvi¹⁰⁸, C. Berat³⁶, X. Bertou¹, P.L. Biermann⁴², P. Billoir³⁵, F. Blanco⁸¹, M. Blanco⁸², C. Bleve³⁸, H. Blümer^{41, 39}, M. Boháčová²⁹, D. Boncioli⁵¹, C. Bonifazi^{25, 35}, R. Bonino⁵⁷, N. Borodai⁷², J. Brack⁹¹, P. Brogueira⁷⁴, W.C. Brown⁹², R. Bruijn⁸⁷, P. Buchholz⁴⁵, A. Bueno⁸³, R.E. Burton⁸⁹, K.S. Caballero-Mora⁹⁹, L. Caramete⁴², R. Caruso⁵², A. Castellina⁵⁷, O. Catalano⁵⁶, G. Cataldi⁴⁹, L. Cazon⁷⁴, R. Cester⁵³, J. Chauvin³⁶, S.H. Cheng⁹⁹, A. Chiavassa⁵⁷, J.A. Chinellato²⁰, A. Chou⁹³, J. Chudoba²⁹, R.W. Clay¹³, M.R. Coluccia⁴⁹, R. Conceição⁷⁴, F. Contreras¹¹, H. Cook⁸⁷, M.J. Cooper¹³, J. Coppens^{68, 70}, A. Cordier³⁴, S. Coutu⁹⁹, C.E. Covault⁸⁹, A. Creusot^{33, 79}, A. Criss⁹⁹, J. Cronin¹⁰¹, A. Curutiu⁴², S. Dagoret-Campagne³⁴, R. Dallier³⁷, S. Dasso^{8, 4}, K. Daumiller³⁹, B.R. Dawson¹³, R.M. de Almeida²⁶, M. De Domenico⁵², C. De Donato^{67, 48}, S.J. de Jong^{68, 70}, G. De La Vega¹⁰, W.J.M. de Mello Junior²⁰, J.R.T. de Mello Neto²⁵, I. De Mitri⁴⁹, V. de Souza¹⁸, K.D. de Vries⁶⁹, G. Decerprit³³, L. del Peral⁸², M. del Río^{51, 11}, O. Deligny³², H. Dembinski⁴¹, N. Dhital⁹⁵, C. Di Giulio^{47, 51}, J.C. Diaz⁹⁵, M.L. Díaz Castro¹⁷, P.N. Diep¹¹⁰, C. Dobrigkeit²⁰, W. Docters⁶⁹, J.C. D'Olivo⁶⁷, P.N. Dong^{110, 32}, A. Dorofeev⁹¹, J.C. dos Anjos¹⁶, M.T. Dova⁷, D. D'Urso⁵⁰, I. Dutan⁴², J. Ebr²⁹, R. Engel³⁹, M. Erdmann⁴³, C.O. Escobar²⁰, J. Espadanal⁷⁴, A. Etchegoyen², P. Facal San Luis¹⁰¹, I. Fajardo Tapia⁶⁷, H. Falcke^{68, 71}, G. Farrar⁹⁶, A.C. Fauth²⁰, N. Fazzini⁹³, A.P. Ferguson⁸⁹, A. Ferrero², B. Fick⁹⁵, A. Filevich², A. Filipčić^{78, 79}, S. Fliescher⁴³, C.E. Fracchiolla⁹¹, E.D. Fraenkel⁶⁹, U. Fröhlich⁴⁵, B. Fuchs¹⁶, R. Gaior³⁵, R.F. Gamarra², S. Gambetta⁴⁶, B. García¹⁰, D. García Gámez^{34, 83}, D. Garcia-Pinto⁸¹, A. Gascon⁸³, H. Gemmeke⁴⁰, K. Gesterling¹⁰⁶, P.L. Ghia^{35, 57}, U. Giaccari⁴⁹, M. Giller⁷³, H. Glass⁹³, M.S. Gold¹⁰⁶, G. Golup¹, F. Gomez Albarracin⁷, M. Gómez Berisso¹, P. Gonçalves⁷⁴, D. Gonzalez⁴¹, J.G. Gonzalez⁴¹, B. Gookin⁹¹, D. Góra^{41, 72}, A. Gorgi⁵⁷, P. Gouffon¹⁹, S.R. Gozzini⁸⁷, E. Grashorn⁹⁸, S. Grebe^{68, 70}, N. Griffith⁹⁸, M. Grigat⁴³, A.F. Grillo⁵⁸, Y. Guardincerri⁴, F. Guarino⁵⁰, G.P. Guedes²¹, A. Guzman⁶⁷, J.D. Hague¹⁰⁶, P. Hansen⁷, D. Harari¹, S. Harmsma^{69, 70}, T.A. Harrison¹³, J.L. Harton⁹¹, A. Haungs³⁹, T. Hebbeker⁴³, D. Heck³⁹, A.E. Herve¹³, C. Hojvat⁹³, N. Hollon¹⁰¹, V.C. Holmes¹³, P. Homola⁷², J.R. Hörandel⁶⁸, A. Horneffer⁶⁸, P. Horvath³⁰, M. Hrabovský^{30, 29}, T. Huege³⁹, A. Insolia⁵², F. Ionita¹⁰¹, A. Italiano⁵², C. Jarne⁷, S. Jiraskova⁶⁸, M. Josebachuili², K. Kadija²⁷, K.H. Kampert³⁸, P. Karhan²⁸, P. Kasper⁹³, B. Kégl³⁴, B. Keilhauer³⁹, A. Keivani⁹⁴, J.L. Kelley⁶⁸, E. Kemp²⁰, R.M. Kieckhafer⁹⁵, H.O. Klages³⁹, M. Kleifges⁴⁰, J. Kleinfeller³⁹, J. Knapp⁸⁷,

D.-H. Koang³⁶, K. Kotera¹⁰¹, N. Krohm³⁸, O. Krömer⁴⁰, D. Kruppke-Hansen³⁸,
 F. Kuehn⁹³, D. Kuempel³⁸, J.K. Kulbartz⁴⁴, N. Kunka⁴⁰, G. La Rosa⁵⁶, C. Lachaud³³,
 P. Lautridou³⁷, M.S.A.B. Leão²⁴, D. Lebrun³⁶, P. Lebrun⁹³, M.A. Leigui de Oliveira²⁴,
 A. Lemiere³², A. Letessier-Selvon³⁵, I. Lhenry-Yvon³², K. Link⁴¹, R. López⁶³, A. Lopez
 Agüera⁸⁴, K. Louedec³⁴, J. Lozano Bahilo⁸³, L. Lu⁸⁷, A. Lucero^{2, 57}, M. Ludwig⁴¹,
 H. Lyberis³², M.C. Maccarone⁵⁶, C. Macolino³⁵, S. Maldera⁵⁷, D. Mandat²⁹, P. Mantsch⁹³,
 A.G. Mariazzi⁷, J. Marin^{11, 57}, V. Marin³⁷, I.C. Maris³⁵, H.R. Marquez Falcon⁶⁶,
 G. Marsella⁵⁴, D. Martello⁴⁹, L. Martin³⁷, H. Martinez⁶⁴, O. Martínez Bravo⁶³,
 H.J. Mathes³⁹, J. Matthews^{94, 100}, J.A.J. Matthews¹⁰⁶, G. Matthiae⁵¹, D. Maurizio⁵³,
 P.O. Mazur⁹³, G. Medina-Tanco⁶⁷, M. Melissas⁴¹, D. Melo^{2, 53}, E. Menichetti⁵³,
 A. Menshikov⁴⁰, P. Mertsch⁸⁵, C. Meurer⁴³, S. Mićanović²⁷, M.I. Micheletti⁹, W. Miller¹⁰⁶,
 L. Miramonti⁴⁸, L. Molina-Bueno⁸³, S. Mollerach¹, M. Monasor¹⁰¹, D. Monnier
 Ragainé³⁴, F. Montanet³⁶, B. Morales⁶⁷, C. Morello⁵⁷, E. Moreno⁶³, J.C. Moreno⁷,
 C. Morris⁹⁸, M. Mostafá⁹¹, C.A. Moura^{24, 50}, S. Mueller³⁹, M.A. Muller²⁰, G. Müller⁴³,
 M. Münchmeyer³⁵, R. Mussa⁵³, G. Navarra^{57 †}, J.L. Navarro⁸³, S. Navas⁸³, P. Necesal²⁹,
 L. Nellen⁶⁷, A. Nelles^{68, 70}, J. Neuser³⁸, P.T. Nhung¹¹⁰, L. Niemietz³⁸, N. Nierstenhoefer³⁸,
 D. Nitz⁹⁵, D. Nosek²⁸, L. Nožka²⁹, M. Nyklicek²⁹, J. Oehlschläger³⁹, A. Olinto¹⁰¹,
 P. Oliva³⁸, V.M. Olmos-Gilbaja⁸⁴, M. Ortiz⁸¹, N. Pacheco⁸², D. Pakk Selmi-Dei²⁰,
 M. Palatka²⁹, J. Pallotta³, N. Palmieri⁴¹, G. Parente⁸⁴, E. Parizot³³, A. Parra⁸⁴,
 R.D. Parsons⁸⁷, S. Pastor⁸⁰, T. Paul⁹⁷, M. Pech²⁹, J. Pękala⁷², R. Pelayo⁸⁴, I.M. Pepe²³,
 L. Perrone⁵⁴, R. Pesce⁴⁶, E. Petermann¹⁰⁵, S. Petrera⁴⁷, P. Petrinca⁵¹, A. Petrolini⁴⁶,
 Y. Petrov⁹¹, J. Petrovic⁷⁰, C. Pfendner¹⁰⁸, N. Phan¹⁰⁶, R. Piegai⁴, T. Pierog³⁹, P. Pieroni⁴,
 M. Pimenta⁷⁴, V. Pirronello⁵², M. Platino², V.H. Ponce¹, M. Pontz⁴⁵, P. Privitera¹⁰¹,
 M. Prouza²⁹, E.J. Quel³, S. Querchfeld³⁸, J. Rautenberg³⁸, O. Ravel³⁷, D. Ravignani²,
 B. Revenu³⁷, J. Ridky²⁹, S. Riggi^{84, 52}, M. Risse⁴⁵, P. Ristori³, H. Rivera⁴⁸, V. Rizzi⁴⁷,
 J. Roberts⁹⁶, C. Robledo⁶³, W. Rodrigues de Carvalho^{84, 19}, G. Rodriguez⁸⁴, J. Rodriguez
 Martino¹¹, J. Rodriguez Rojo¹¹, I. Rodriguez-Cabo⁸⁴, M.D. Rodríguez-Frías⁸², G. Ros⁸²,
 J. Rosado⁸¹, T. Rossler³⁰, M. Roth³⁹, B. Rouillé-d'Orfeuille¹⁰¹, E. Roulet¹, A.C. Rovero⁸,
 C. Rühle⁴⁰, F. Salamida^{47, 39}, H. Salazar⁶³, F. Salesa Greus⁹¹, G. Salina⁵¹, F. Sánchez²,
 C.E. Santo⁷⁴, E. Santos⁷⁴, E.M. Santos²⁵, F. Sarazin⁹⁰, B. Sarkar³⁸, S. Sarkar⁸⁵, R. Sato¹¹,
 N. Scharf⁴³, V. Scherini⁴⁸, H. Schieler³⁹, P. Schiffer⁴³, A. Schmidt⁴⁰, F. Schmidt¹⁰¹,
 O. Scholten⁶⁹, H. Schoorlemmer^{68, 70}, J. Schovancova²⁹, P. Schovánek²⁹, F. Schröder³⁹,
 S. Schulte⁴³, D. Schuster⁹⁰, S.J. Sciutto⁷, M. Scuderi⁵², A. Segreto⁵⁶, M. Settimo⁴⁵,
 A. Shadkam⁹⁴, R.C. Shellard^{16, 17}, I. Sidelnik², G. Sigl⁴⁴, H.H. Silva Lopez⁶⁷,
 A. Śmiałkowski⁷³, R. Šmída^{39, 29}, G.R. Snow¹⁰⁵, P. Sommers⁹⁹, J. Sorokin¹³,
 H. Spinka^{88, 93}, R. Squartini¹¹, S. Stanic⁷⁹, J. Stapleton⁹⁸, J. Stasielak⁷², M. Stephan⁴³,
 E. Strazzeri⁵⁶, A. Stutz³⁶, F. Suarez², T. Suomijärvi³², A.D. Supanitsky^{8, 67}, T. Šuša²⁷,
 M.S. Sutherland^{94, 98}, J. Swain⁹⁷, Z. Szadkowski⁷³, M. Szuba³⁹, A. Tamashiro⁸, A. Tapia²,
 M. Tartare³⁶, O. Taşcău³⁸, C.G. Tavera Ruiz⁶⁷, R. Tcaciuc⁴⁵, D. Tegolo^{52, 61}, N.T. Thao¹¹⁰,
 D. Thomas⁹¹, J. Tiffenberg⁴, C. Timmermans^{70, 68}, D.K. Tiwari⁶⁶, W. Tkaczyk⁷³,
 C.J. Todero Peixoto^{18, 24}, B. Tomé⁷⁴, A. Tonachini⁵³, P. Travnicek²⁹, D.B. Tridapalli¹⁹,
 G. Tristram³³, E. Trovato⁵², M. Tueros^{84, 4}, R. Ulrich^{99, 39}, M. Unger³⁹, M. Urban³⁴,
 J.F. Valdés Galicia⁶⁷, I. Valiño^{84, 39}, L. Valore⁵⁰, A.M. van den Berg⁶⁹, E. Varela⁶³,
 B. Vargas Cárdenas⁶⁷, J.R. Vázquez⁸¹, R.A. Vázquez⁸⁴, D. Veberič^{79, 78}, V. Verzi⁵¹,
 J. Vicha²⁹, M. Videla¹⁰, L. Villaseñor⁶⁶, H. Wahlberg⁷, P. Wahrlich¹³, O. Wainberg²,

D. Walz⁴³, D. Warner⁹¹, A.A. Watson⁸⁷, M. Weber⁴⁰, K. Weidenhaupt⁴³, A. Weindl³⁹,
S. Westerhoff¹⁰⁸, B.J. Whelan¹³, G. Wieczorek⁷³, L. Wiencke⁹⁰, B. Wilczyńska⁷²,
H. Wilczyński⁷², M. Will³⁹, C. Williams¹⁰¹, T. Winchen⁴³, M.G. Winnick¹³,
M. Wommer³⁹, B. Wundheiler², T. Yamamoto^{101 a}, T. Yapici⁹⁵, P. Younk⁴⁵, G. Yuan⁹⁴,
A. Yushkov^{84, 50}, B. Zamorano⁸³, E. Zas⁸⁴, D. Zavrtnik^{79, 78}, M. Zavrtnik^{78, 79}, I. Zaw⁹⁶,
A. Zepeda⁶⁴, M. Zimbres Silva^{38, 20}, M. Ziolkowski⁴⁵

¹ Centro Atómico Bariloche and Instituto Balseiro (CNEA- UNCuyo-CONICET), San Carlos de Bariloche, Argentina

² Centro Atómico Constituyentes (Comisión Nacional de Energía Atómica/CONICET/UTN-FRBA), Buenos Aires, Argentina

³ Centro de Investigaciones en Láseres y Aplicaciones, CITEFA and CONICET, Argentina

⁴ Departamento de Física, FCEyN, Universidad de Buenos Aires y CONICET, Argentina

⁷ IFLP, Universidad Nacional de La Plata and CONICET, La Plata, Argentina

⁸ Instituto de Astronomía y Física del Espacio (CONICET- UBA), Buenos Aires, Argentina

⁹ Instituto de Física de Rosario (IFIR) - CONICET/U.N.R. and Facultad de Ciencias Bioquímicas y Farmacéuticas U.N.R., Rosario, Argentina

¹⁰ National Technological University, Faculty Mendoza (CONICET/CNEA), Mendoza, Argentina

¹¹ Observatorio Pierre Auger, Malargüe, Argentina

¹² Observatorio Pierre Auger and Comisión Nacional de Energía Atómica, Malargüe, Argentina

¹³ University of Adelaide, Adelaide, S.A., Australia

¹⁶ Centro Brasileiro de Pesquisas Físicas, Rio de Janeiro, RJ, Brazil

¹⁷ Pontifícia Universidade Católica, Rio de Janeiro, RJ, Brazil

¹⁸ Universidade de São Paulo, Instituto de Física, São Carlos, SP, Brazil

¹⁹ Universidade de São Paulo, Instituto de Física, São Paulo, SP, Brazil

²⁰ Universidade Estadual de Campinas, IFGW, Campinas, SP, Brazil

²¹ Universidade Estadual de Feira de Santana, Brazil

²² Universidade Estadual do Sudoeste da Bahia, Vitória da Conquista, BA, Brazil

²³ Universidade Federal da Bahia, Salvador, BA, Brazil

²⁴ Universidade Federal do ABC, Santo André, SP, Brazil

²⁵ Universidade Federal do Rio de Janeiro, Instituto de Física, Rio de Janeiro, RJ, Brazil

²⁶ Universidade Federal Fluminense, EEIMVR, Volta Redonda, RJ, Brazil

²⁷ Rudjer Bošković Institute, 10000 Zagreb, Croatia

²⁸ Charles University, Faculty of Mathematics and Physics, Institute of Particle and Nuclear Physics, Prague, Czech Republic

²⁹ Institute of Physics of the Academy of Sciences of the Czech Republic, Prague, Czech Republic

³⁰ Palacky University, RCATM, Olomouc, Czech Republic

³² Institut de Physique Nucléaire d'Orsay (IPNO), Université Paris 11, CNRS-IN2P3, Orsay, France

³³ Laboratoire AstroParticule et Cosmologie (APC), Université Paris 7, CNRS-IN2P3, Paris, France

³⁴ Laboratoire de l'Accélérateur Linéaire (LAL), Université Paris 11, CNRS-IN2P3,

Orsay, France

- ³⁵ Laboratoire de Physique Nucléaire et de Hautes Energies (LPNHE), Universités Paris 6 et Paris 7, CNRS-IN2P3, Paris, France
- ³⁶ Laboratoire de Physique Subatomique et de Cosmologie (LPSC), Université Joseph Fourier, INPG, CNRS-IN2P3, Grenoble, France
- ³⁷ SUBATECH, École des Mines de Nantes, CNRS-IN2P3, Université de Nantes, Nantes, France
- ³⁸ Bergische Universität Wuppertal, Wuppertal, Germany
- ³⁹ Karlsruhe Institute of Technology - Campus North - Institut für Kernphysik, Karlsruhe, Germany
- ⁴⁰ Karlsruhe Institute of Technology - Campus North - Institut für Prozessdatenverarbeitung und Elektronik, Karlsruhe, Germany
- ⁴¹ Karlsruhe Institute of Technology - Campus South - Institut für Experimentelle Kernphysik (IEKP), Karlsruhe, Germany
- ⁴² Max-Planck-Institut für Radioastronomie, Bonn, Germany
- ⁴³ RWTH Aachen University, III. Physikalisches Institut A, Aachen, Germany
- ⁴⁴ Universität Hamburg, Hamburg, Germany
- ⁴⁵ Universität Siegen, Siegen, Germany
- ⁴⁶ Dipartimento di Fisica dell'Università and INFN, Genova, Italy
- ⁴⁷ Università dell'Aquila and INFN, L'Aquila, Italy
- ⁴⁸ Università di Milano and Sezione INFN, Milan, Italy
- ⁴⁹ Dipartimento di Fisica dell'Università del Salento and Sezione INFN, Lecce, Italy
- ⁵⁰ Università di Napoli "Federico II" and Sezione INFN, Napoli, Italy
- ⁵¹ Università di Roma II "Tor Vergata" and Sezione INFN, Roma, Italy
- ⁵² Università di Catania and Sezione INFN, Catania, Italy
- ⁵³ Università di Torino and Sezione INFN, Torino, Italy
- ⁵⁴ Dipartimento di Ingegneria dell'Innovazione dell'Università del Salento and Sezione INFN, Lecce, Italy
- ⁵⁶ Istituto di Astrofisica Spaziale e Fisica Cosmica di Palermo (INAF), Palermo, Italy
- ⁵⁷ Istituto di Fisica dello Spazio Interplanetario (INAF), Università di Torino and Sezione INFN, Torino, Italy
- ⁵⁸ INFN, Laboratori Nazionali del Gran Sasso, Assergi (L'Aquila), Italy
- ⁶¹ Università di Palermo and Sezione INFN, Catania, Italy
- ⁶³ Benemérita Universidad Autónoma de Puebla, Puebla, Mexico
- ⁶⁴ Centro de Investigación y de Estudios Avanzados del IPN (CINVESTAV), México, D.F., Mexico
- ⁶⁶ Universidad Michoacana de San Nicolas de Hidalgo, Morelia, Michoacan, Mexico
- ⁶⁷ Universidad Nacional Autónoma de México, México, D.F., México
- ⁶⁸ IMAPP, Radboud University Nijmegen, Netherlands
- ⁶⁹ Kernfysisch Versneller Instituut, University of Groningen, Groningen, Netherlands
- ⁷⁰ Nikhef, Science Park, Amsterdam, Netherlands
- ⁷¹ ASTRON, Dwingeloo, Netherlands
- ⁷² Institute of Nuclear Physics PAN, Krakow, Poland
- ⁷³ University of Łódź, Łódź, Poland
- ⁷⁴ LIP and Instituto Superior Técnico, Technical University of Lisbon, Portugal

- ⁷⁸ J. Stefan Institute, Ljubljana, Slovenia
- ⁷⁹ Laboratory for Astroparticle Physics, University of Nova Gorica, Slovenia
- ⁸⁰ Instituto de Física Corpuscular, CSIC-Universitat de València, Valencia, Spain
- ⁸¹ Universidad Complutense de Madrid, Madrid, Spain
- ⁸² Universidad de Alcalá, Alcalá de Henares (Madrid), Spain
- ⁸³ Universidad de Granada & C.A.F.P.E., Granada, Spain
- ⁸⁴ Universidad de Santiago de Compostela, Spain
- ⁸⁵ Rudolf Peierls Centre for Theoretical Physics, University of Oxford, Oxford, United Kingdom
- ⁸⁷ School of Physics and Astronomy, University of Leeds, United Kingdom
- ⁸⁸ Argonne National Laboratory, Argonne, IL, USA
- ⁸⁹ Case Western Reserve University, Cleveland, OH, USA
- ⁹⁰ Colorado School of Mines, Golden, CO, USA
- ⁹¹ Colorado State University, Fort Collins, CO, USA
- ⁹² Colorado State University, Pueblo, CO, USA
- ⁹³ Fermilab, Batavia, IL, USA
- ⁹⁴ Louisiana State University, Baton Rouge, LA, USA
- ⁹⁵ Michigan Technological University, Houghton, MI, USA
- ⁹⁶ New York University, New York, NY, USA
- ⁹⁷ Northeastern University, Boston, MA, USA
- ⁹⁸ Ohio State University, Columbus, OH, USA
- ⁹⁹ Pennsylvania State University, University Park, PA, USA
- ¹⁰⁰ Southern University, Baton Rouge, LA, USA
- ¹⁰¹ University of Chicago, Enrico Fermi Institute, Chicago, IL, USA
- ¹⁰⁵ University of Nebraska, Lincoln, NE, USA
- ¹⁰⁶ University of New Mexico, Albuquerque, NM, USA
- ¹⁰⁸ University of Wisconsin, Madison, WI, USA
- ¹⁰⁹ University of Wisconsin, Milwaukee, WI, USA
- ¹¹⁰ Institute for Nuclear Science and Technology (INST), Hanoi, Vietnam
- (†) Deceased
- (a) at Konan University, Kobe, Japan
- (f) now at University of Maryland

Abstract

We present a comprehensive study of the influence of the geomagnetic field on the energy estimation of extensive air showers with a zenith angle smaller than 60° , detected at the Pierre Auger Observatory. The geomagnetic field induces an azimuthal modulation of the estimated energy of cosmic rays up to the $\sim 2\%$ level at large zenith angles. We present a method to account for this modulation of the reconstructed energy. We analyse the effect of the modulation on large scale anisotropy searches in the arrival direction distributions of cosmic rays. At a given energy, the geomagnetic effect is shown to induce a pseudo-dipolar

pattern at the percent level in the declination distribution that needs to be accounted for.

1. Introduction

High energy cosmic rays generate extensive air showers in the atmosphere. The trajectories of the charged particles of the showers are curved in the Earth's magnetic field, resulting in a broadening of the spatial distribution of particles in the direction of the Lorentz force. While such effects are known to distort the particle densities in a dramatic way at zenith angles larger than $\sim 60^\circ$ [1–4], they are commonly ignored at smaller zenith angles where the lateral distribution function is well described by empirical models of the NKG-type [5, 6] based on a radial symmetry of the distribution of particles in the plane perpendicular to the shower axis.

In this article, we aim to quantify the small changes of the particle densities at ground induced by the geomagnetic field for showers with zenith angle smaller than $\sim 60^\circ$, focusing on the impacts on the energy estimator used at the Pierre Auger Observatory. As long as the magnitude of these effects lies well below the statistical uncertainty of the energy reconstruction, it is reasonable to neglect them in the framework of the energy spectrum reconstruction. As the strength of the geomagnetic field component perpendicular to the arrival direction of the cosmic ray, B_T , depends on both the zenith and the azimuthal angles (θ, φ) of any incoming shower, these effects are expected to break the symmetry of the energy estimator in terms of the azimuthal angle φ . Such an azimuthal dependence translates into azimuthal modulations of the estimated cosmic ray event rate at a given energy. For any observatory located far from the Earth's poles, any genuine large scale pattern which depends on the declination translates also into azimuthal modulations of the cosmic ray event rate. Thus to perform a large scale anisotropy measurement it is critical to account for azimuthal modulations of experimental origin and for those induced by the geomagnetic field, as already pointed out in the analysis of the Yakutsk data [7]. Hence, this work constitutes an accompanying paper of a search for large scale anisotropies, both in right ascension and declination of cosmic rays detected at the Pierre Auger Observatory, the results of which will be reported in a forthcoming publication.

To study the influence of the geomagnetic field on the cosmic ray energy estimator, we make use of shower simulations and of the measurements performed with the surface detector array of the Pierre Auger Observatory, located in Malargüe, Argentina (35.2°S , 69.5°W) at 1400 m a.s.l. [8]. The Pierre Auger Observatory is designed to study cosmic rays (CRs) with energies above $\sim 10^{18}$ eV. The surface detector array consists of 1660 water Cherenkov detectors sensitive to the photons and the charged particles of the showers. It is laid out over an area of 3000 km^2 on a triangular grid and is overlooked by four fluorescence detectors. The energy at which the detection efficiency of the surface detector array saturates is $\sim 3\text{ EeV}$ [9]. For each event, the signals recorded in the stations are fitted to find the signal at 1000 m from the shower core, $S(1000)$, used as a measure of the shower size. The shower size $S(1000)$ is converted to the value S_{38} that would have been expected had the shower arrived at a zenith angle of 38° . S_{38} is then converted into energy using a calibration curve based on the fluorescence telescope measurements [10].

The influence of the geomagnetic field on the spatial distribution of particles for showers with zenith angle less than 60° is presented in Section 2, through a toy model aimed

43 at explaining the directional dependence of the shower size $S(1000)$ induced by the geo-
 44 magnetic field. The observation of this effect in the data of the Pierre Auger Observatory
 45 is reported in Section 3. In Section 4, we quantify the size of the $S(1000)$ distortions
 46 with zenith and azimuthal angles by means of end-to-end shower simulations, and then
 47 present the procedure to convert the shower size corrected for the geomagnetic effects into
 48 energy using the Constant Intensity Cut method. In Section 5, the consequences on large
 49 scale anisotropies are discussed, while systematic uncertainties associated with the primary
 50 mass, the primary energy and the number of muons in showers are presented in Section 6.

51 **2. Influence of the geomagnetic field on extensive air showers**

52 The interaction of a primary cosmic ray in the atmosphere produces mostly charged
 53 and neutral pions, initiating a hadronic cascade. The decay of neutral pions generates the
 54 electromagnetic component of the shower, while the decay of the charged pions generates
 55 the muonic one. Electrons undergo stronger scattering, so that the electron distribution is
 56 only weakly affected by the geomagnetic deflections. Muons are produced with a typical
 57 energy E_μ of a few GeV (increasing with the altitude of production). The decay angle
 58 between pions and muons is causing only a small additional random deflection, as they
 59 almost inherit the transverse momentum p_T of their parents (a few hundred MeV/c) so that
 60 the distance of the muons from the shower core scales as the inverse of their energy. While
 61 the radial offset of the pions from the shower axis is of the order of a few 10 m, it does
 62 not contribute significantly to the lateral distribution of the muons observed on the ground
 63 at distances $r \geq 100$ m. Hence, at ground level, the angular spread of the muons around
 64 the shower axis can be considered as mainly caused by the transverse momentum inherited
 65 from the parental pions.

66 After their production, muons are affected by ionisation and radiative energy losses,
 67 decay, multiple scattering and geomagnetic deflections. Below 100 GeV, the muon energy
 68 loss is mainly due to ionisation and is relatively small (amounting to about $2 \text{ MeV g}^{-1} \text{ cm}^2$),
 69 allowing a large fraction of muons to reach the ground before decaying. Multiple scattering
 70 in the electric field of air nuclei randomises the directions of muons to some degree, but
 71 the contribution to the total angular divergence of the muons from the shower axis remains
 72 small up to zenith angles of the shower-axis of about 80° .

73 Based on these general considerations, we now introduce a simple toy model aimed at
 74 understanding the main features of the muon density distortions induced by the geomag-
 75 netic field. We adopt the shower front plane coordinate system depicted in Fig. 1 [2]. In
 76 the absence of the magnetic field, and neglecting multiple scattering, a relativistic muon
 77 of energy $E_\mu \simeq cp_\mu$ and transverse momentum p_T will reach the shower front plane after
 78 traveling a distance d at a position r from the shower axis given by

$$r \simeq \frac{p_T}{p_\mu} d \simeq \frac{cp_T}{E_\mu} d. \quad (1)$$

79 On the other hand, in the presence of the magnetic field, muons suffer additional geomag-

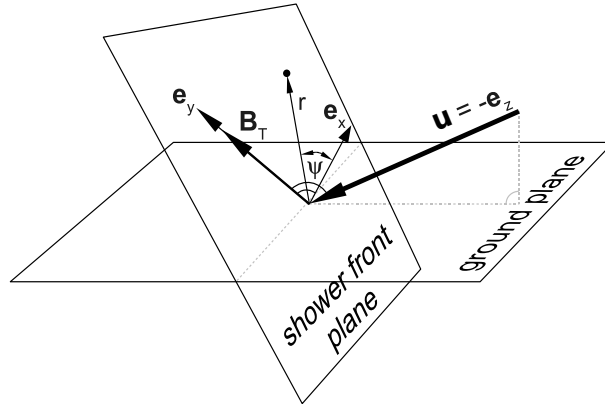


Figure 1: The shower front plane coordinate system [2, 4]: \mathbf{e}_z is anti-parallel to the shower direction \mathbf{u} , while \mathbf{e}_y is parallel to \mathbf{B}_T , the projection of the magnetic field \mathbf{B} onto the shower plane x - y . (ψ, r) are the polar coordinates in the shower plane.

netic deflections. We treat the geomagnetic field \mathbf{B} in Malargüe as a constant field¹,

$$B = 24.6 \mu\text{T}, \quad D_B = 2.6^\circ, \quad I_B = -35.2^\circ, \quad (2)$$

D_B and I_B being the geomagnetic declination and inclination. The deflection of a relativistic muon in the presence of a magnetic field with transverse component B_T can be approximated with

$$\delta x_{\pm} \simeq \pm \frac{ecB_T d^2}{2E_{\mu}}, \quad (3)$$

where e is the elementary electric charge and the sign corresponds to positive/negative charged muons. The dependence of the geomagnetic deflections $\delta x \equiv \delta x_+ = -\delta x_-$ on the distance to the shower axis $r = \sqrt{x^2 + y^2}$ is illustrated in Fig. 2 obtained by comparing the position of the same muons in the presence or in the absence of the geomagnetic field in a simulated vertical shower of a proton at 5 EeV. The deviations expected from the expression for δx_{\pm} are also shown in the same graph (solid line). It was obtained by inserting muon energy and distance at the production point of the simulated muons into Eq. (3). It turns out that Eq. (3) estimates rather well the actual deviations, though the distance between the actual and the predicted deviations increases at large r . This is mainly because on the one hand d underestimates the actual travel length to a larger extent at larger r , while on the other hand the magnetic deviation actually increases while muons gradually lose energy during travel. Hence, from the muon density $\rho_{\mu}(x, y)$ in the transverse plane in the absence of the geomagnetic field, the corresponding density $\bar{\rho}_{\mu}(\bar{x}, \bar{y})$ in the presence of such a field can be obtained by making the following Jacobian transformation, in the same way as in the framework of very inclined showers [2],

$$\bar{\rho}_{\mu}(\bar{x}, \bar{y}) = \left| \frac{\partial(x, y)}{\partial(\bar{x}, \bar{y})} \right| \rho_{\mu}(x(\bar{x}, \bar{y}), y(\bar{x}, \bar{y})). \quad (4)$$

¹In Malargüe the geomagnetic field has varied by about 1° in direction and 2% in magnitude over 10 years [11].

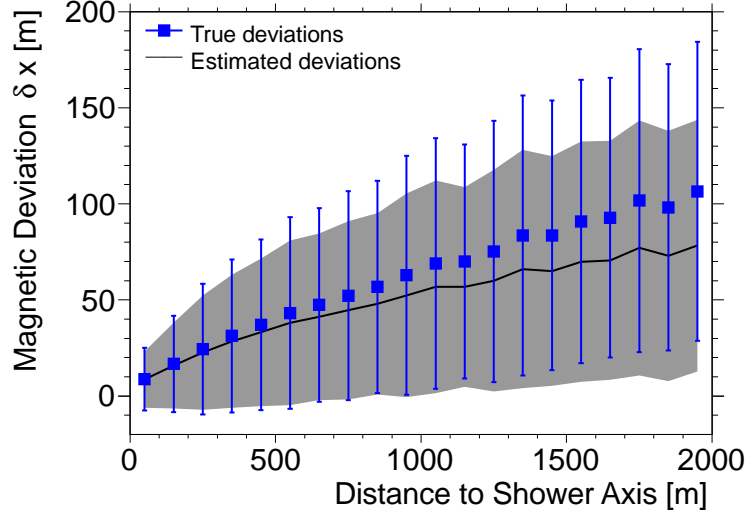


Figure 2: Magnetic deviations as a function of the distance to the shower axis observed on a simulated vertical shower (points). Superimposed are the deviations expected from Eq. (3) (line). The shaded region and the error bars give the corresponding dispersion.

99 Here, the term “muon density” refers to the time-integrated muon flux through the trans-
 100 verse shower front plane associated to the air shower, and the barred coordinates represent
 101 the positions of the muons in the transverse plane in the presence of the geomagnetic field:

$$\begin{aligned}\bar{x} &= x + \delta x_{\pm}(x, y), \\ \bar{y} &= y.\end{aligned}\quad (5)$$

102 Since Eq. (4) induces changes of the shower size $S(1000)$, it is of particular interest to get
 103 an approximate relationship between ρ and $\bar{\rho}$ around 1000 m. From Fig. 2, it is apparent
 104 that around 1000 m the mean magnetic deviation is approximately constant over a distance
 105 range larger than the size of the deviation. When focusing on the changes of density at
 106 1000 m from the shower core, it is thus reasonable to neglect the x and y dependence of the
 107 deviation δx_{\pm} , which allows an approximation of the density $\bar{\rho}_{\mu}(\bar{x}, \bar{y})$ around 1000 m as

$$\begin{aligned}\bar{\rho}_{\mu}(\bar{x}, \bar{y}) &\simeq \rho_{\mu_+}(\bar{x} - \delta x_+, \bar{y}) + \rho_{\mu_-}(\bar{x} - \delta x_-, \bar{y}) \\ &\simeq \rho_{\mu}(\bar{x}, \bar{y}) + \frac{(\delta x)^2}{2} \frac{\partial^2 \rho_{\mu}}{\partial \bar{x}^2}(\bar{x}, \bar{y}),\end{aligned}\quad (6)$$

108 where we assumed $\rho_{\mu_-} = \rho_{\mu_+} = \rho_{\mu}/2$. The two opposite muon charges cancel out the
 109 linear term in δx and we see that magnetic effects change the muon density around 1000 m
 110 by a factor proportional to $(\delta x)^2 \propto B_T^2 \propto \sin^2(\widehat{\mathbf{u}, \mathbf{b}})$, where \mathbf{u} and $\mathbf{b} = \mathbf{B}/|B|$ denote the
 111 unit vectors in the shower direction and the magnetic field direction, respectively. This is
 112 particularly important with regard to the azimuthal behaviour of the effect, as the azimuthal
 113 dependence is contained *only* in the $B_T^2(\theta, \varphi)$ term. This dependency is therefore a generic
 114 expectation outlined by this toy model. The model will be verified in Section 4 by making
 115 use of complete simulation of showers. On the other hand, the zenith angle dependence
 116 relies on other ingredients that we will probe in an accurate way in Section 4, such as the
 117 altitude distribution of the muon production and the muon energy distribution.

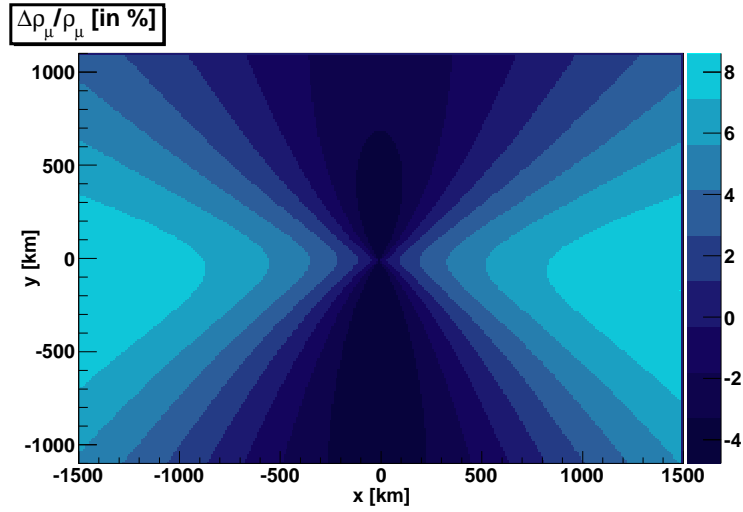


Figure 3: Relative changes of $\Delta\rho_\mu/\rho_\mu$ in the transverse shower front plane due to the presence of the geomagnetic field, obtained at zenith angle $\theta = 60^\circ$ and azimuthal angle aligned along $D_B + 180^\circ$.

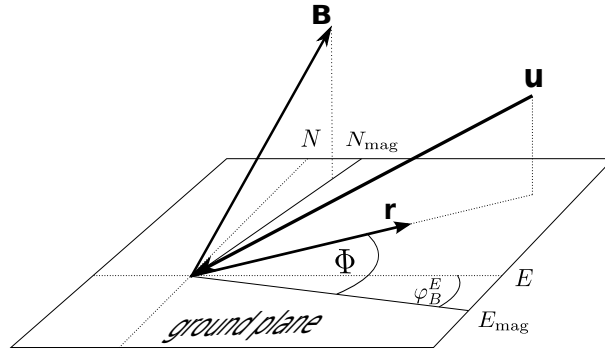


Figure 4: Definition of angle Φ with respect to the magnetic East E_{mag} and the shower core for a given shower direction \mathbf{u} and a surface detector at \mathbf{r} . The azimuthal angle of the magnetic field vector \mathbf{B} defines the magnetic North N_{mag} .

118 3. Observation of geomagnetic effects in the Pierre Auger Observatory data

119 To illustrate the differences between $\bar{\rho}_\mu$ and ρ_μ described in Eq. (4), the relative changes
 120 $\Delta\rho_\mu/\rho_\mu$ are shown in Fig. 3 in the transverse shower front plane by producing muon maps
 121 from simulations at zenith angle $\theta = 60^\circ$ and azimuthal angle aligned along $D_B + 180^\circ$
 122 in the presence and in the absence of the geomagnetic field. A predominant quadrupolar
 123 asymmetry at the few percent level is visible, corresponding to the separation of positive
 124 and negative charges in the direction of the Lorentz force.

125 This quadrupolar asymmetry is expected to induce to some extent a quadrupolar modu-
 126 lation of the surface detector signals as a function of the *polar angle on the ground*, defined
 127 here as the angle between the axis given by the shower core and the surface detector, and
 128 the magnetic East $\varphi_B^E = -D_B = -2.6^\circ$ (Fig. 4). The use of this particular angle, instead
 129 of the polar angle ψ which is defined in the *shower front plane* (see Fig. 1), allows us to
 130 remove dipolar asymmetries in the surface detector signals, the origin of which is related

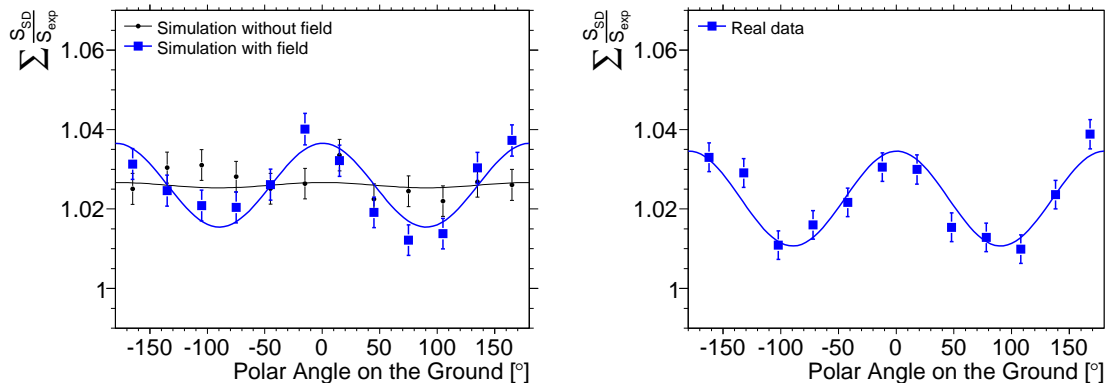


Figure 5: Average ratio of the true signal in each surface detector with respect to the expected one as a function of the polar angle on the ground. Left panel: using simulated showers in the presence (thick points) and in the absence (thin points) of the geomagnetic field. Right panel: using real data above 4 EeV. The solid lines give the fit of a quadrupolar modulation to the corresponding points.

131 to the radial divergence of particles from the shower axis. Such asymmetries cancel out in
 132 this analysis, due to the isotropic distribution of the cosmic rays. To demonstrate the geo-
 133 magnetic effect, we produced a realistic Monte-Carlo simulation using 30 000 isotropically
 134 distributed showers (with zenith angles less than 60°) with random core positions within
 135 the array. The injected primary energies were chosen to be greater than 4 EeV (safely
 136 excluding angle dependent trigger probability) and distributed according to a power law
 137 energy spectrum $dN/dE \propto E^{-\gamma}$ with power index $\gamma = 2.7$, so that this shower library is
 138 as close as possible to the real data set. To each shower we apply the reconstruction pro-
 139 cedure of the surface detector, leading to a fit of the lateral distribution function [10]. The
 140 lateral distribution function parametrizes the signal strength in the shower plane, assuming
 141 circular shower symmetry. By evaluating the lateral distribution function at the position of
 142 the surface detector, we obtain the expected signal S_{exp} . This signal can be compared to
 143 the true signal in the surface detector S_{SD} . The ratio between the observed and expected
 144 signals as a function of the polar angle on the ground in simulated showers is shown in
 145 the left panel of Fig. 5, with (thick points) and without (thin points) the geomagnetic field.
 146 While a significant quadrupolar modulation with a fixed phase along D_B and amplitude
 147 $\simeq (1.1 \pm 0.2)\%$ is observed when the field is on, no such modulation is observed when the
 148 field is off ($\simeq (0.1 \pm 0.2)\%$), as expected. In the right panel, the same analysis is performed
 149 on the real data above 4 EeV, including again about 30 000 showers. A significant mod-
 150 ulation of $\simeq (1.2 \pm 0.2)\%$ is observed, agreeing both in amplitude and phase within the
 151 uncertainties with the simulations performed *in the presence* of the geomagnetic field. This
 152 provides clear hints of the influence of the geomagnetic field in the Auger data.

153 Note that this analysis is restricted to surface detectors that are more than 1000 m away
 154 from the shower core. This cut is motivated by Fig. 3, showing that the quadrupolar am-
 155 plitude is larger at large distances from the shower core. We further require the surface
 156 detectors to have signals larger than 4 VEM^2 . This cut is a compromise between keeping

²VEM - Vertical Equivalent Muon - is the average charge corresponding to the Cherenkov light produced

157 good statistics and keeping trigger effects small. Above 4 VEM the measured amplitude
 158 does not depend systematically on the signal strength cut. However a cut in the surface
 159 detector signals induces a statistical trigger bias because showers with upward signal fluc-
 160 tuations will trigger more readily. This explains the small discrepancy between real and
 161 Monte-Carlo data in terms of the global normalisation in Fig. 5 which differs from 1 by
 162 $\sim 3\%$. Cutting at larger signals reduces this discrepancy.

163 Most importantly, depending on the incoming direction, the quadrupolar asymmetry
 164 is also expected to affect the shower size $S(1000)$ and thus the energy estimator as qual-
 165 itatively described in Eq. (6). Consequently, these effects are expected to modulate the
 166 estimated cosmic ray event rate at a given energy as a function of the incoming direction,
 167 and in particular to generate a North/South asymmetry in the azimuthal distribution³. Such
 168 an asymmetry is also expected in the case of a *genuine* large scale modulation of the flux
 169 of cosmic rays. However related analyses of the azimuthal distribution are out of the scope
 170 of this paper, and we restrict ourselves in the rest of this article to present a comprehensive
 171 study of the geomagnetic distortions of the energy estimator. This will allow us to apply the
 172 corresponding corrections in a forthcoming publication aimed at searching for large scale
 173 anisotropies.

174 4. Geomagnetic distortions of the energy estimator

175 4.1. Geomagnetic distortions of the shower size $S(1000)$

176 The toy model presented in Section 2 allows us to understand the main features of
 177 the influence of the geomagnetic field on the muonic component of extensive air showers.
 178 To get an accurate estimation of the distortions induced by the field on the shower size
 179 $S(1000)$ as a function of both the zenith and the azimuthal angles, we present here the
 180 results obtained by means of end-to-end simulations of proton-initiated showers generated
 181 with the AIRES program [13] and with the hadronic interaction model QGSJET [14]. We
 182 have checked that the results obtained with the CORSIKA program [15] are compatible. We
 183 consider a fixed energy $E = 5 \text{ EeV}$ and seven fixed zenith angles between $\theta = 0^\circ$ and $\theta =$
 184 60° . The dependency of the effect in terms of the primary mass and of the number of muons
 185 in showers as well as its evolution with energy are sources of systematic uncertainties. The
 186 influence of such systematics will be quantified in Section 6. Within our convention for the
 187 azimuthal angle, the azimuthal direction of the magnetic North is $\varphi_B^N = 90^\circ - D_B = 87.4^\circ$.
 188 The zenith direction of the field is $\theta_B = 90^\circ - |I_B| = 54.8^\circ$.

189 To verify the predicted behaviour of the shower size shift in terms of B_T^2 , we first show
 190 the results of the simulations of 1000 showers at a zenith angle $\theta = \theta_B$ and for two distinct
 191 azimuthal angles $\varphi = \varphi_B^N$ and $\varphi = \varphi_B^N + 90^\circ$. Each shower is then thrown 10 times at the
 192 surface detector array with random core positions and reconstructed using exactly the same
 193 reconstruction procedure as the one applied to real data. For this specific zenith angle θ_B ,
 194 no shift is expected in the North direction φ_B^N as the transverse component of the magnetic

by a vertical and central through-going muon in the surface detector. It is the unit used in the evaluation of the signal recorded by the detectors [12].

³The convention we use for the azimuthal angle φ is to define it relative to the East direction, counter-clockwise.

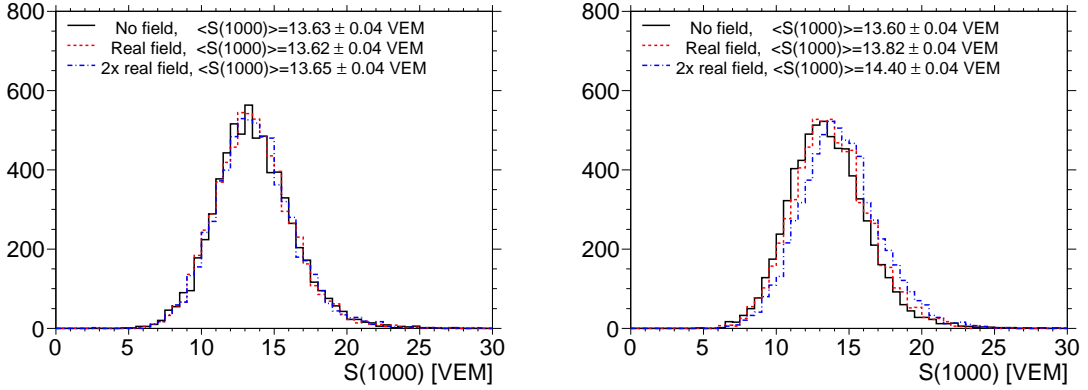


Figure 6: Distributions of shower size $S(1000)$ obtained by simulating showers at zenith angle $\theta = \theta_B$ and azimuthal angle φ_B^N (left) and $\varphi_B^N + 90^\circ$ (right). Thick histogram: no magnetic field. Dotted histogram: real magnetic field in Malargüe. Dashed histogram: twice the real magnetic field in Malargüe.

195 field is zero. This is indeed the case as illustrated in the left panel of Fig. 6, showing
 196 the distribution of reconstructed $S(1000)$ for three different configurations of the magnetic
 197 field: no field, real field in Malargüe, and twice the real field in Malargüe. It can be seen
 198 that on average all histograms are – within the statistical uncertainties on the average –
 199 centered on the same value. In the right panel of Fig. 6 we repeat the same analysis with
 200 the showers generated in the direction $\varphi_B^N + 90^\circ$. Since the transverse component of the field
 201 is now different from zero, a clear relative shift in terms of $\Delta S(1000)/S(1000)$ is observed
 202 between the three distributions: the shift is $\simeq 1.6\%$ between the configurations with and
 203 without the field, leading to a discrimination with a significance of $\simeq 5.5\sigma$, while the shift
 204 is $\simeq 6\%$ between the configurations with twice the real field and without the field leading
 205 to a discrimination with a significance of $\simeq 20\sigma$. It can be noticed that the strength of the
 206 shift is thus in overall agreement with the expected scaling B_T^2 .

207 For the zenith angle $\theta = \theta_B$, in Fig. 7 we show the shift of the mean $S(1000)$ ob-
 208 tained by simulating 1000 showers in the same way as previously for eight different values
 209 of the azimuth angle. Again, the results are displayed for configurations with the real
 210 field (bottom) and with twice the real field (top). The expected behaviours in terms of
 211 $\Delta S(1000)/S(1000) = G(\theta_B) \sin^2(\widehat{\mathbf{u}, \mathbf{b}})$ are shown by the continuous curves, where the nor-
 212 malisation factor G is tuned by hand. Clearly, the shape of the curves agrees remarkably
 213 well with the Monte Carlo data within the uncertainties. Hence, this study supports the
 214 claim that the azimuthal dependence of the shift in $S(1000)$ induced by the magnetic field
 215 is proportional to $B_T^2(\theta, \varphi)$, in agreement with the expectations provided by general consid-
 216 erations expressed in the previous section on the muonic component of the showers.

217 The B_T^2 term encompassing the overall azimuthal dependence at each zenith angle, the
 218 remaining shift $G(\theta) = \Delta S(1000)/S(1000)/\sin^2(\widehat{\mathbf{u}, \mathbf{b}})$ depends on the zenith angle through
 219 the altitude distribution of the muon production, the muon energy distribution, and the
 220 weight of the muonic contribution to the shower size $S(1000)$. Repeating the simulations
 221 at different zenith angles, we plot G as a function of the zenith angle in Fig. 8. Due to
 222 the increased travel lengths of the muons and due to their larger relative contribution to

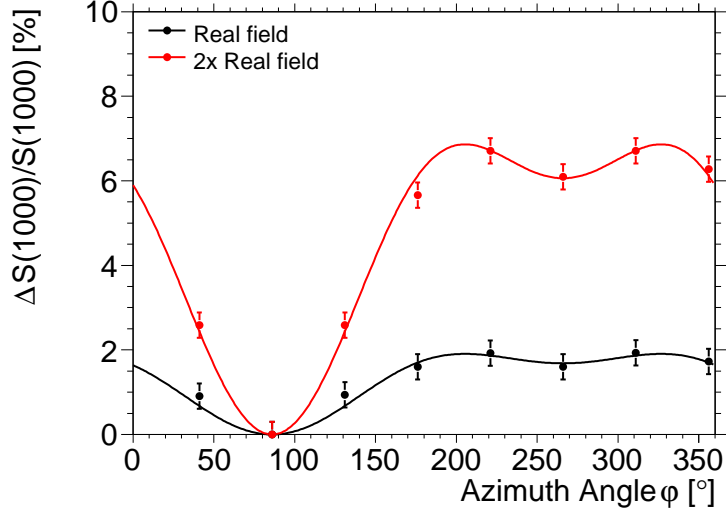


Figure 7: $\Delta S(1000)/S(1000)$ (in %) as a function of the azimuthal angle φ , at zenith angle $\theta = \theta_B$ for two different field strengths. Points are obtained by Monte Carlo shower simulation, lines are the expected behavior (see Section 2).

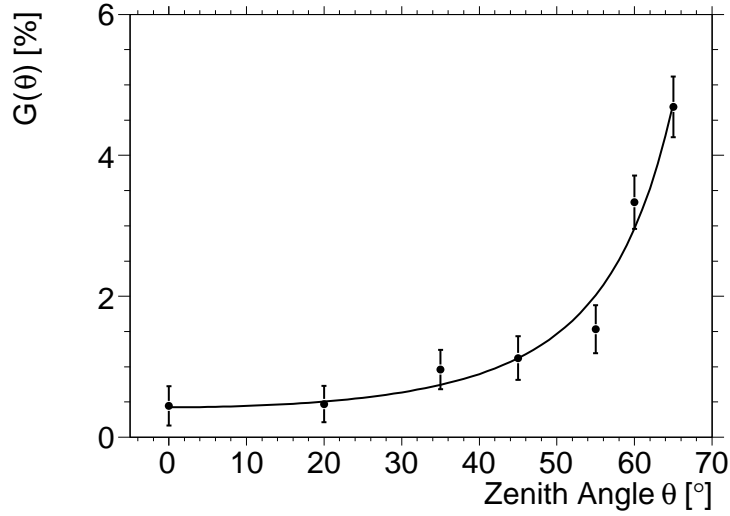


Figure 8: $G(\theta) = \Delta S(1000)/S(1000)/\sin^2(\widehat{\mathbf{u}, \mathbf{b}})$ as a function of the zenith angle θ .

223 $S(1000)$ at high zenith angles, the value of G rises rapidly for angles above $\simeq 40^\circ$. The
 224 superimposed curve is an *empirical* fit, allowing us to get the following parametrisation of
 225 the shower size distortions induced by the geomagnetic field,

$$\frac{\Delta S(1000)}{S(1000)}(\theta, \varphi) = 4.2 \cdot 10^{-3} \cos^{-2.8} \theta \sin^2(\widehat{\mathbf{u}, \mathbf{b}}). \quad (7)$$

226 4.2. From shower size to energy

227 At the Pierre Auger Observatory, the shower size $S(1000)$ is converted into energy E
 228 using a two-step procedure [10]. First, the evolution of $S(1000)$ with zenith angle arising

229 from the attenuation of the shower with increasing atmospheric thickness is quantified by
 230 applying the *Constant Intensity Cut* (CIC) method that is based on the (at least approximate)
 231 isotropy of incoming cosmic rays. The CIC relates relates $S(1000)$ in vertical and inclined
 232 showers through a line of equal intensity in spectra at different zenith angles. This allows
 233 us to correct the value of $S(1000)$ for attenuation by computing its value had the shower ar-
 234 rived from a fixed zenith angle, here 38 degrees (corresponding to the median of the angular
 235 distribution of events for energies greater than 3 EeV). This zenith angle independent esti-
 236 mator S_{38} is defined as $S_{38} = S(1000)/CIC(\theta)$. The calibration of S_{38} with energy E is then
 237 achieved using a relation of the form $E = AS_{38}^B$, where $A = 1.49 \pm 0.06(\text{stat}) \pm 0.12(\text{syst})$
 238 and $B = 1.08 \pm 0.01(\text{stat}) \pm 0.04(\text{syst})$ were estimated from the correlation between S_{38}
 239 and E in a subset of high quality "hybrid events" measured simultaneously by the surface
 240 detector (SD) and the fluorescence detector (FD) [10]. In such a sample, S_{38} and E are
 241 independently measured, with S_{38} from the SD and E from the FD.

242 This two-step procedure has an important consequence on the implementation of the
 243 energy corrections for the geomagnetic effects. The CIC curve is constructed assuming
 244 that the shower size estimator $S(1000)$ does not depend on the azimuthal angle. The in-
 245 duced azimuthal variation of $S(1000)$ due to the geomagnetic effect is thus averaged while
 246 the zenith angle dependence of the geomagnetic effects is absorbed when the CIC is imple-
 247 mented. To illustrate this in a simplified way, consider the case in which the magnetic field
 248 were directed along the zenith direction (*i.e.* in the case of a virtual Observatory located at
 249 the Southern magnetic pole) so that the transverse component of the magnetic field would
 250 not depend on the azimuthal direction of any incoming shower. Then the shift in $S(1000)$
 251 would depend *only* on the zenith angle in such a way that the Constant Intensity Cut method
 252 would by construction absorb the shift induced by $G(\theta)$ into the empirical $CIC(\theta)$ curve,
 253 while the empirical relationship $E = AS_{38}^B$ would calibrate S_{38} into energy with no need for
 254 any additional corrections.

255 This leads us to implement the energy corrections for geomagnetic effects, relating the
 256 energy E_0 reconstructed ignoring the geomagnetic effects to the *corrected* energy E by

$$E = \frac{E_0}{(1 + \Delta(\theta, \varphi))^B}, \quad (8)$$

257 with

$$\Delta(\theta, \varphi) = G(\theta) \left[\sin^2(\widehat{\mathbf{u}, \mathbf{b}}) - \langle \sin^2(\widehat{\mathbf{u}, \mathbf{b}}) \rangle_\varphi \right] \quad (9)$$

258 where $\langle \cdot \rangle_\varphi$ denotes the average over φ and where B is one of the parameters used in the S_{38}
 259 to E conversion described above. This expression implies that energies are *under-estimated*
 260 preferentially for showers coming from the northern directions of the array, while they
 261 are *over-estimated* for showers coming from the southern directions, the size of the effect
 262 increasing with the zenith angle.

263 5. Consequences for large scale anisotropy searches

264 5.1. Impact on the estimated event rate

265 To provide an illustration of the impact of the energy corrections for geomagnetic ef-
 266 fects, we calculate here, as a function of declination δ , the deviation of the event rate $N_0(\delta)$,

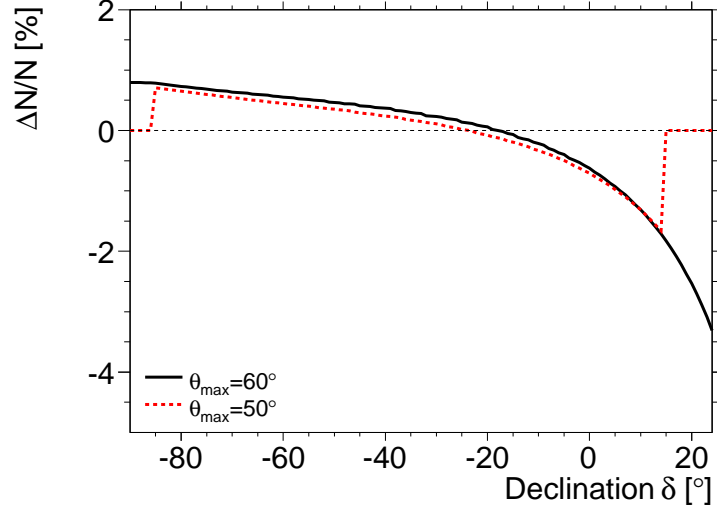


Figure 9: Relative differences $\Delta N/N$ as a function of the declination, for 2 different values of θ_{\max} .

267 measured if we were not to implement the corrections of the energy estimator by Eq. (8),
 268 to the event rate $N(\delta)$ expected from an isotropic background distribution.

269 The “canonical exposure” [16] holds for a full-time operation of the surface detector
 270 array above the energy at which the detection efficiency is saturated over the considered
 271 zenith range. In such a case, the directional detection efficiency is simply proportional to
 272 $\cos \theta$,

$$\omega(\theta) \propto \cos(\theta) H(\theta - \theta_{\max}) \quad (10)$$

273 where H is the Heaviside function and θ_{\max} is the maximal zenith angle considered. The
 274 zenith angle is related to the declination δ and the right ascension α through

$$\cos \theta = \sin \ell_{\text{site}} \sin \delta + \cos \ell_{\text{site}} \cos \delta \cos \alpha \quad (11)$$

275 where ℓ_{site} is the Earth’s latitude of the Observatory. The event rate at a given declination δ
 276 and above an energy threshold E_{th} is obtained by integrating in energy and right ascension
 277 α ,

$$N(\delta) \propto \int_{E_{\text{th}}}^{\infty} dE \int_0^{2\pi} d\alpha \omega(\theta) \frac{dN(\theta, \varphi, E)}{dE} \quad (12)$$

278 Note that at lower energies this integral acquires an additional energy and angle dependent
 279 detection efficiency term $\epsilon(E, \theta, \phi)$. Hereafter we assume that the cosmic ray spectrum
 280 is a power law, *i.e.* $dN/dE \propto E^{-\gamma}$. From Eq. (8) it follows that if the effect of the
 281 geomagnetic field were not accounted for, the measured energy spectrum would have a
 282 directional modulation given by

$$\frac{dN}{dE_0} \propto [1 + \Delta(\theta, \varphi)]^{B(\gamma-1)} E_0^{-\gamma}. \quad (13)$$

283 This leads to the following measured event rate above a given uncorrected energy E_{th} ,

$$N_0(\delta) \propto \int_{E_{\text{th}}}^{\infty} dE_0 \int_0^{2\pi} d\alpha H(\cos \theta - \cos \theta_{\max}) \cos \theta [1 + \Delta(\theta, \varphi)]^{B(\gamma-1)} E_0^{-\gamma}, \quad (14)$$

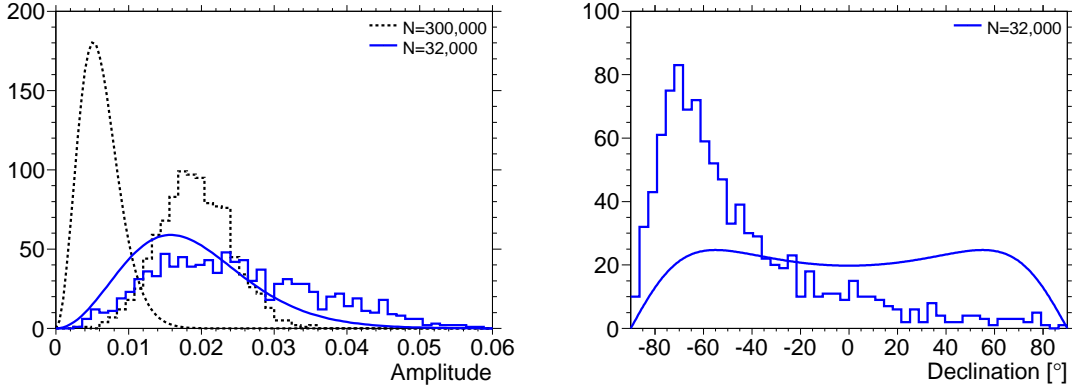


Figure 10: Dipolar reconstruction of arrival directions of mock data sets with event rates distorted by the geomagnetic effects. Left: distributions of amplitudes. Right: distributions of declinations. The smooth lines give the expected distribution in the case of isotropy.

284 where φ is related to α and δ through

$$\tan \varphi = \frac{\sin \delta \cos \ell_{\text{site}} - \cos \delta \cos \alpha \sin \ell_{\text{site}}}{\cos \delta \sin \alpha}. \quad (15)$$

285 The event rate $N_0(\delta)$ as a function of declination is then calculated using Eq. (13) in Eq.
 286 (12). The relative difference $\Delta N/N$ is shown in Fig. 9 as a function of the declination, with
 287 spectral index $\gamma = 2.7$. The energy over-estimation (under-estimation) of events coming
 288 preferentially from the Southern (Northern) azimuthal directions, as described in Eq. (8),
 289 leads to an effective excess (deficit) of the event rate for $\delta \lesssim -20^\circ$ ($\delta \gtrsim -20^\circ$), with an
 290 amplitude of $\simeq 2\%$ when considering $\theta_{\text{max}} = 60^\circ$. It is worth noting that this amplitude is
 291 reduced to within 1% when considering $\theta_{\text{max}} = 50^\circ$, as shown by the dotted line.

292 5.2. Impact on dipolar modulation searches

293 The pattern displayed in Fig. 9 roughly imitates a dipole with an amplitude at the per-
 294 cent level. To evaluate precisely the impact of this pattern on the assessment of a dipole
 295 moment in the reconstructed arrival directions and to probe the statistics needed for the
 296 sensitivity to such a spurious pattern, we apply the multipolar reconstruction adapted to the
 297 case of a partial sky coverage [17] to mock data sets by limiting the maximum bound of the
 298 expansion L_{max} to 1 (pure dipolar reconstruction). Since the distortions are axisymmetric
 299 around the axis defined by the North and South celestial poles, only the multipolar coef-
 300 ficient related to this particular axis is expected to be affected (here: a_{10}). Consequently,
 301 this particular coefficient has impacts on both the amplitude of the reconstructed dipole and
 302 its direction with respect to the axis defined by the North and South celestial poles (the
 303 technical details of relating the estimation of the multipolar coefficients to the spherical
 304 coordinates of a dipole are given in the Appendix).

305 To simulate the directional distortions induced by Eq. (8), each mock data set is drawn
 306 from the event rate $N_0(\delta)$ corresponding to the uncorrected energies, and is reconstructed
 307 using the canonical exposure in Eq. (10). The results of this procedure applied to 1000
 308 samples are shown in Fig. 10. In the left panel, the distribution of the reconstructed am-
 309 plitudes r using $N = 300\,000$ events is shown by the dotted histogram. It clearly deviates

310 from the expected isotropic distribution displayed as the dotted curve which corresponds to
 311 (see Appendix)

$$p_R(r) = \frac{r}{\sigma \sqrt{\sigma_z^2 - \sigma^2}} \operatorname{erfi}\left(\frac{\sqrt{\sigma_z^2 - \sigma^2}}{\sigma \sigma_z} \frac{r}{\sqrt{2}}\right) \exp\left(-\frac{r^2}{2\sigma^2}\right), \quad (16)$$

312 where $\operatorname{erfi}(z) = \operatorname{erf}(iz)/i$, and where the width parameters σ and σ_z can be calculated
 313 from the exposure function [17]. With the particular exposure function used here, it turns
 314 out that $\sigma \simeq 1.02 \sqrt{3/N}$ and $\sigma_z \simeq 1.59 \sqrt{3/N}$. This allows us to estimate the spurious
 315 dipolar amplitude⁴ to be of the order of the mean of the dotted histogram, about $\simeq 1.9\%$.
 316 Consequently, we can estimate that the spurious effect becomes predominant as soon as the
 317 mean noise amplitude $\langle r \rangle$ deduced from Eq. (16) is of the order of 1.9%,

$$\langle r \rangle = \sqrt{\frac{2}{\pi}} \left(\sigma_z + \frac{\sigma^2 \operatorname{arctanh}(\sqrt{1 - \sigma^2/\sigma_z^2})}{\sqrt{\sigma_z^2 - \sigma^2}} \right) \simeq 1.9\%. \quad (17)$$

318 This translates into the condition $N \simeq 32\,000$ (solid histogram). Using such a number of
 319 events, the bias induced on the amplitude reconstruction is illustrated in the same graph
 320 by the longer tail of the full histogram with respect to the expected one, and is even more
 321 evident in the right panel of Fig. 10, showing the distribution of the reconstructed decli-
 322 nation direction of the dipole which already deviates to a large extent from the expected
 323 distribution.

324 6. Systematic uncertainties

325 The parametrisation of $G(\theta)$ in Eq. (7) was obtained by means of simulations of proton
 326 showers at a fixed energy. The height of the first interaction influences the production
 327 altitude of muons detected at 1000 m from the shower core at the ground level. Moreover,
 328 as muons are produced at the end of the hadronic cascade, when the energy of the charged
 329 mesons is diminished so much that their decay length becomes smaller than their interaction
 330 length (which is inversely proportional to the air density), the energy distribution of muons
 331 is also affected by the height of the first interaction. Because the air density is lower in
 332 the upper atmosphere, this mechanism results in an increase of the energy of muons. The
 333 muonic contribution to $S(1000)$ depends also on both the primary mass and primary energy.
 334 For all these reasons, the parametrisation of $G(\theta)$ is expected to depend on both the primary
 335 mass and primary energy.

336 To probe these influences, we repeat the same chain of end-to-end simulations using
 337 proton showers at energies of 50 EeV and iron showers at 5 EeV. Results in terms of the
 338 distortions of the observed event rate $N(\delta)$ are shown in Fig. 11. We also display in the
 339 same graph the results obtained using the hadronic interaction model QGSJETII [18]. The

⁴Due to the partial sky exposure considered here, the estimate of the dipolar amplitude is biased by the higher multipolar orders needed to fully describe $\Delta N/N$ shown in Fig. 10 [17]. The aim of this calculation is only to provide a quantitative illustration of the spurious measurement which would be performed due to the geomagnetic effects when reconstructing a pure dipolar pattern.

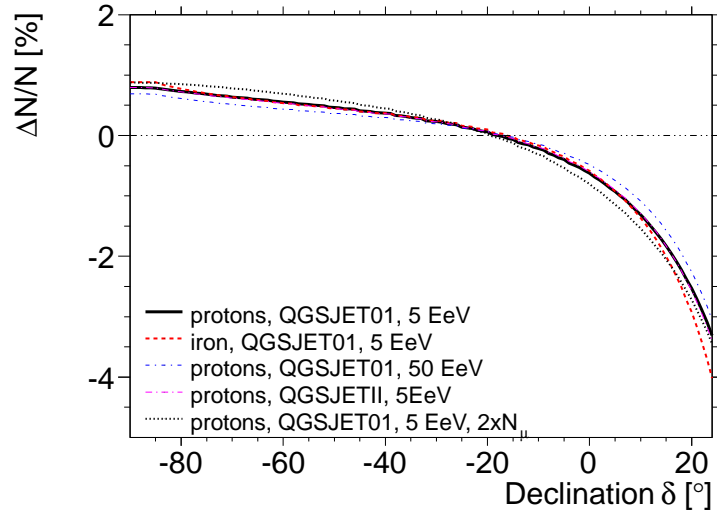


Figure 11: Relative differences $\Delta N/N$ as a function of the declination, for different primary masses, different primary energies, different hadronic models and for increased number of muons in showers.

340 differences with respect to the reference model are small, so that the consequences on large
 341 scale anisotropy searches presented in Section 5 remain unchanged within the statistics
 342 available at the Pierre Auger Observatory.

343 In addition, there are discrepancies in the hadronic interaction model predictions re-
 344 garding the number of muons in shower simulations and what is found in our data [19].
 345 Higher number of muons influences the weight of the muonic contribution to $S(1000)$. The
 346 consequences of increasing the number of muons by a factor of 2 on the distortions of the
 347 observed event rate are also shown in Fig. 11. As the muonic contribution to $S(1000)$ is
 348 already large at high zenith angles in the reference model, this increase of the number of
 349 muons does not lead to large differences.

350 7. Conclusion

351 In this work, we have identified and quantified a systematic uncertainty affecting the
 352 energy determination of cosmic rays detected by the surface detector array of the Pierre
 353 Auger Observatory. This systematic uncertainty, induced by the influence of the geomag-
 354 netic field on the shower development, has a strength which depends on both the zenith
 355 and the azimuthal angles. Consequently, we have shown that it induces distortions of the
 356 estimated cosmic ray event rate at a given energy at the percent level in both the azimuthal
 357 and the declination distributions, the latter of which mimics an almost dipolar pattern.

358 We have also shown that the induced distortions are already at the level of the statistical
 359 uncertainties for a number of events $N \approx 32\,000$ (we note that the full Auger surface
 360 detector array collects about 6500 events per year with energies above 3 EeV). Accounting
 361 for these effects is thus essential with regard to the correct interpretation of large scale
 362 anisotropy measurements taking explicitly profit from the declination distribution.

363 Acknowledgements

364 The successful installation, commissioning, and operation of the Pierre Auger Obser-
365 vatory would not have been possible without the strong commitment and effort from the
366 technical and administrative staff in Malargüe.

367 We are very grateful to the following agencies and organizations for financial support:
368 Comisión Nacional de Energía Atómica, Fundación Antorchas, Gobierno De La Provincia
369 de Mendoza, Municipalidad de Malargüe, NDM Holdings and Valle Las Leñas, in grati-
370 tude for their continuing cooperation over land access, Argentina; the Australian Research
371 Council; Conselho Nacional de Desenvolvimento Científico e Tecnológico (CNPq), Fi-
372 nanciadora de Estudos e Projetos (FINEP), Fundação de Amparo à Pesquisa do Estado
373 de Rio de Janeiro (FAPERJ), Fundação de Amparo à Pesquisa do Estado de São Paulo
374 (FAPESP), Ministério de Ciência e Tecnologia (MCT), Brazil; AVCR AV0Z10100502 and
375 AV0Z10100522, GAAV KJB100100904, MSMT-CR LA08016, LC527, 1M06002, and
376 MSM0021620859, Czech Republic; Centre de Calcul IN2P3/CNRS, Centre National de
377 la Recherche Scientifique (CNRS), Conseil Régional Ile-de-France, Département Physique
378 Nucléaire et Corpusculaire (PNC-IN2P3/CNRS), Département Sciences de l'Univers (SDU-
379 INSU/CNRS), France; Bundesministerium für Bildung und Forschung (BMBF), Deutsche
380 Forschungsgemeinschaft (DFG), Finanzministerium Baden-Württemberg, Helmholtz-Gemeinschaft
381 Deutscher Forschungszentren (HGF), Ministerium für Wissenschaft und Forschung, Nordrhein-
382 Westfalen, Ministerium für Wissenschaft, Forschung und Kunst, Baden-Württemberg, Ger-
383 many; Istituto Nazionale di Fisica Nucleare (INFN), Ministero dell'Istruzione, dell'Università
384 e della Ricerca (MIUR), Italy; Consejo Nacional de Ciencia y Tecnología (CONACYT),
385 Mexico; Ministerie van Onderwijs, Cultuur en Wetenschap, Nederlandse Organisatie voor
386 Wetenschappelijk Onderzoek (NWO), Stichting voor Fundamenteel Onderzoek der Ma-
387 terie (FOM), Netherlands; Ministry of Science and Higher Education, Grant Nos. N
388 N202 200239 and N N202 207238, Poland; Fundação para a Ciência e a Tecnologia,
389 Portugal; Ministry for Higher Education, Science, and Technology, Slovenian Research
390 Agency, Slovenia; Comunidad de Madrid, Consejería de Educación de la Comunidad de
391 Castilla La Mancha, FEDER funds, Ministerio de Ciencia e Innovación and Consolider-
392 Ingenio 2010 (CPAN), Xunta de Galicia, Spain; Science and Technology Facilities Council,
393 United Kingdom; Department of Energy, Contract Nos. DE-AC02-07CH11359, DE-FR02-
394 04ER41300, National Science Foundation, Grant No. 0450696, The Grainger Foundation
395 USA; ALFA-EC / HELEN, European Union 6th Framework Program, Grant No. MEIF-
396 CT-2005-025057, European Union 7th Framework Program, Grant No. PIEF-GA-2008-
397 220240, and UNESCO.

398 Appendix

399 The p.d.f. of the first harmonic amplitude for a data set of N points drawn at random
400 over a circle is known to be the Rayleigh distribution. In this appendix, we generalise
401 this distribution to the case of N points being drawn at random on the sphere over the
402 exposure $\omega(\delta)$ of the Pierre Auger Observatory. Assuming the underlying arrival direction
403 distribution to be of the form $\Phi(\alpha, \delta) = \Phi_0(1 + \mathbf{D} \cdot \mathbf{u})$, the components of the dipolar vector

404 **D** are related to the multipolar coefficients through

$$D_x = \sqrt{3} \frac{a_{11}}{a_{00}}, \quad D_y = \sqrt{3} \frac{a_{1-1}}{a_{00}}, \quad D_z = \sqrt{3} \frac{a_{10}}{a_{00}}. \quad (18)$$

405 Denoting by x, y, z the estimates of D_x, D_y, D_z , the joint p.d.f. $p_{X,Y,Z}(x, y, z)$ can be factorised
 406 in the limit of large number of events in terms of three centered Gaussian distributions
 407 $N(0, \sigma)$,

$$p_{X,Y,Z}(x, y, z) = p_X(x)p_Y(y)p_Z(z) = N(0, \sigma_x)N(0, \sigma_y)N(0, \sigma_z), \quad (19)$$

408 where the standard deviation parameters can be calculated from the exposure function [17].
 409 With the particular exposure function used here, it turns out that numerical integrations lead
 410 to $\sigma \simeq 1.02 \sqrt{3/N}$ and $\sigma_z \simeq 1.59 \sqrt{3/N}$. The joint p.d.f. $p_{R,\Delta,A}(r, \delta, \alpha)$ expressing the dipole
 411 components in spherical coordinates is obtained from Eq. (19) by performing the Jacobian
 412 transformation

$$\begin{aligned} p_{R,\Delta,A}(r, \delta, \alpha) &= \left| \frac{\partial(x, y, z)}{\partial(r, \delta, \alpha)} \right| p_{X,Y,Z}(x(r, \delta, \alpha), y(r, \delta, \alpha), z(r, \delta, \alpha)) \\ &= \frac{r^2 \cos \delta}{(2\pi)^{3/2} \sigma^2 \sigma_z} \exp \left[-\frac{r^2 \cos^2 \delta}{2\sigma^2} - \frac{r^2 \sin^2 \delta}{2\sigma_z^2} \right]. \end{aligned} \quad (20)$$

413 From this joint p.d.f., the p.d.f. of the dipole amplitude (declination) is finally obtained by
 414 marginalising over the other variables, yielding

$$\begin{aligned} p_R(r) &= \frac{r}{\sigma \sqrt{\sigma_z^2 - \sigma^2}} \operatorname{erfi} \left(\frac{\sqrt{\sigma_z^2 - \sigma^2}}{\sigma \sigma_z} \frac{r}{\sqrt{2}} \right) \exp \left(-\frac{r^2}{2\sigma^2} \right), \\ p_\Delta(\delta) &= \frac{\sigma \sigma_z^2 \cos \delta}{2 (\sigma_z^2 \cos^2 \delta + \sigma^2 \sin^2 \delta)^{3/2}}. \end{aligned} \quad (21)$$

415 Finally, one can derive from p_R quantities of interest, such as the expected mean noise $\langle r \rangle$,
 416 the RMS σ_r and the probability of obtaining an amplitude greater than r :

$$\langle r \rangle = \sqrt{\frac{2}{\pi}} \left(\sigma_z + \frac{\sigma^2 \operatorname{arctanh}(\sqrt{1 - \sigma^2/\sigma_z^2})}{\sqrt{\sigma_z^2 - \sigma^2}} \right), \quad (22)$$

$$\sigma_r = \sqrt{2\sigma^2 + \sigma_z^2 - \langle r \rangle^2}, \quad (23)$$

$$\operatorname{Prob}(> r) = \operatorname{erfc} \left(\frac{r}{\sqrt{2}\sigma_z} \right) + \frac{\sigma}{\sqrt{\sigma_z^2 - \sigma^2}} \operatorname{erfi} \left(\frac{\sqrt{\sigma_z^2 - \sigma^2}}{\sqrt{2}\sigma \sigma_z} r \right) \exp \left(-\frac{r^2}{2\sigma^2} \right), \quad (24)$$

417 which are the equivalent to the well known Rayleigh formulas $\langle r \rangle = \sqrt{\pi/N}$, $\sigma_r = \sqrt{(4 - \pi)/N}$
 418 and $\operatorname{Prob}(> r) = \exp(-Nr^2/4)$ when dealing with N points drawn at random over a cir-
 419 cle [20].

420 Acknowledgments

421 [1] D. M. Edge *et al.*, J. Phys. A 6 (1973) 1612.

- 422 [2] M. Ave, R. A. Vazquez, and E. Zas, *Astropart. Phys.* 14 (2000) 91.
- 423 [3] M. Ave *et al.*, *Astropart. Phys.* 14 (2000) 109.
- 424 [4] H. Dembinski *et al.*, *Astropart. Phys.* 34 (2010) 128.
- 425 [5] K. Greisen, *Ann. Rev. Nuc. Sci.* 10 (1960) 63.
- 426 [6] K. Kamata and J. Nishimura, *Prog. Theor. Phys.* 6 (1958) 93.
- 427 [7] A. Ivanov *et al.*, *JETP Letters* 69 (1999) 288.
- 428 [8] J. Abraham *et al.* [Pierre Auger Collaboration], *Nucl. Instrum. Meth. A* 523 (2004)
429 50.
- 430 [9] J. Abraham *et al.* [Pierre Auger Collaboration], *Nucl. Instr. and Meth. A* 613 (2010)
431 29-39.
- 432 [10] J. Abraham *et al.* [Pierre Auger Collaboration], *Phys. Rev. Lett.* 101 (2008) 061101.
- 433 [11] National Geography Data Center, <http://www.ngdc.noaa.gov/seg/geomag/geomag.shtml>,
434 2007.
- 435 [12] X. Bertou, et al., Pierre Auger Collaboration, *Nucl. Instr. and Meth. A* 568 (2006)
436 839.
- 437 [13] S.J. Sciutto, Proceedings of the 27th ICRC, Hamburg, Germany, arXiv:astro-
438 ph/0106044v1.
- 439 [14] N.N. Kalmykov and S.S. Ostapchenko, *Yad. Fiz.* 56 (1993) 105; N.N. Kalmykov,
440 S.S. Ostapchenko, and A.I. Pavlov, *Nucl. Phys. B Proc. Suppl.* 52B (1997) 17.
- 441 [15] D. Heck *et al.*, Report FZKA 6019, Karlsruhe, Germany, 1998.
- 442 [16] P. Sommers, *Astropart. Phys.* 14 (2001) 271.
- 443 [17] P. Billoir and O. Deligny, *JCAP* 02 (2008) 009.
- 444 [18] S.S. Ostapchenko, *Nucl. Phys. B Proc. Suppl.* 151 (2006) 147-150.
- 445 [19] R. Engel for the Pierre Auger collaboration, Proceedings of the 30th ICRC, Merida,
446 Mexico, arXiv:0706.1921.
- 447 [20] J. Linsley, *Phys. Rev. Lett.* 34 (1975) 1530.